4 Experiments in Supersonic Flows

Fundamental performance demonstrations of the ALTP represent a series of stagnation-point heat-transfer measurements described in the following chapter. The stagnation point of blunt-body probes is very suitable for quantitative heat-flux measurements because well defined and repeatable flow conditions allow a comparison with theoretical relations and other established measurement techniques. The first experiments using the ALTP heat-flux gauge are carried out in the supersonic short duration wind tunnel (Stoßwindkanal) of IAG. These quantitative short term measurements cover magnitudes of convective heat loads up to $\sim 1\,\mathrm{W/cm^2}$.
The second section provides a demonstration of the ALTP to operate in high-enthalpy partially or fully ionized plasma. Radial heat-flux profiles were measured in the plume of a two-stage hybrid electric thruster by means of a cooled stagnation-point probe. Heat loads up to $\sim 30\,\mathrm{W/cm^2}$ are experienced in this harsh environment. Investigations simulating higher convective heat loads up to $\sim 250\,\mathrm{W/cm^2}$ at M=12 are presented in Section 5.1 under hypersonic flow.
Another fundamental investigation of the ALTP focussed on the characterization of its dynamic properties is carried out on the side wall of a shock tube. Besides the investigation of the boundary layer transition behind a traveling shock wave in a unit Reynolds number regime up to $11 \times 10^6/\mathrm{m}$, the signal response to the passing shock wave is used to obtain amplitude frequency response characteristics. The results are compared to theoretical estimations and radiative sine-wave excitation (sec. 2.8). Furthermore, the optimal size of the protective coatings is studied in these experiments.

4.1 Stagnation-Point Heat-Flux Measurements at M=2.5

4.1.1 Theoretical Relations.

In general, the convective heat transfer rate is approximately proportional to the difference between surface temperature T_w at the body and the recovery temperature T_r of the flow,

when viscous dissipation like in BL flow is significant. In the case where such a dissipation can be neglected as in the stagnation BL, the approximate relationship between heat flux per unit area q and the driving temperature difference is

$$q = h(T_0 - T_w). \tag{4.1}$$

The convective heat transfer coefficient h in the stagnation point of a blunt body is a property of the stagnation-point boundary layer and thus a function of probe geometry and the upstream flow conditions. For a flow with low free-stream turbulence, h can be expressed in dimensionless form of a Nusselt number, which is depending on Prandtl and Reynolds number (White [149]).

$$Nu = B\, Pr^{0.4} Re^{0.5} \left(\frac{\rho_w \mu_w}{\rho_e \mu_e}\right)^{0.1} c_p(T_w - T_e), \tag{4.2}$$

where B is a dimensionless constant, specific for body shape; $K = (d\,u_e/d\,s)$ is the stagnation point velocity gradient (SPVG) and D the probe body diameter. When dissociation of the gas can be excluded, relation 4.1 and 4.2 result in the following correlation for heat transfer rate in the stagnation point derived by Fay and Riddell [33]

$$q_w = B\, Pr^{-0.6} (\rho_e \mu_e K)^{0.5} \left(\frac{\rho_w \mu_w}{\rho_e \mu_e}\right)^{0.1} (\chi_e - \chi_w) \tag{4.3}$$

where the enthalpy difference $(\chi_e - \chi_w) = c_p(T_r - T_w)$ assuming constant c_p and $T_e = T_r$. The heat transfer in the stagnation point depends strongly upon K. The local velocity gradient at the stagnation point of typical bodies depends on body diameter D and velocity u and, to a lesser extent upon the approach Mach number M and the particular

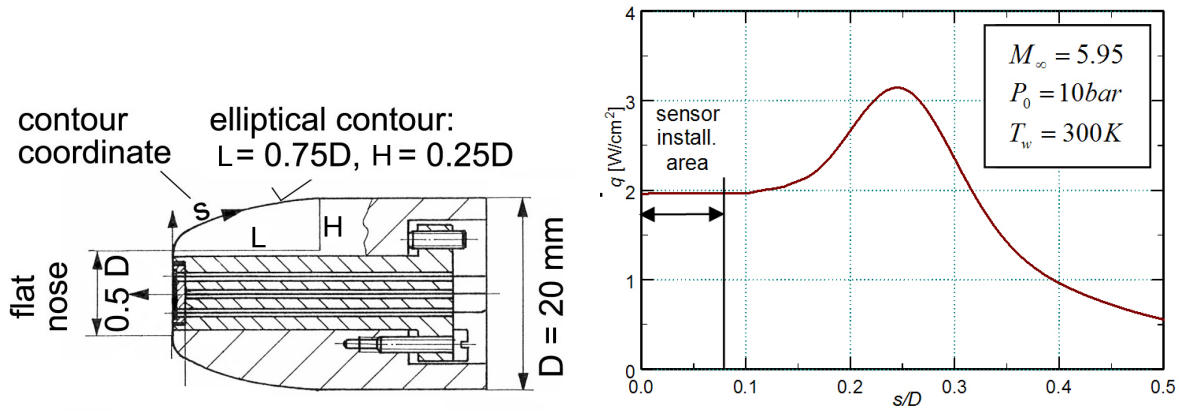

(a) (b)

Figure 4.1: (a) Contour of the small blunt body probe (D=20 mm); (b) Wall heat-flux distribution along the surface contour of the large probe (D=40 mm).

body shape. The SPVG of some basic shapes can be found in Trimmer et al. [78]. The K-value of other shapes, like the one specially designed to incorporate the ALTP, has to be determined from experiments or BL computations.

4.1.2 Probe Body Design.

Figure 4.1(a) shows the contour of the blunt body probes used in the experiments. The flat front surface area of the blunt bodies meets two requirements. On one hand, a sufficiently large planar surface is realized in order to mount a planar ALTP sensor module. Thus, a distortion of the curvature by a step or roughness at the edges of the insert is avoided. On the other hand, the BL development in the stagnation point region of such a flat nose results into an extended radial area of constant heat flux. Hence, the gradient of the radial heat-flux distribution (Fig. 4.1(b)) that could lead to systematic errors in the comparison of measurement techniques with different active areas, is minimized. The specific contour shape is realized for cylindrical probes with two different diameters of 20 and 40 mm. Simultaneous measurements with probes of different diameters allows an inherent confirmation of the ratio of measured stagnation-point heat loads. For example, a diameter ratio of the large to small probe body of 2:1 should results into a $\sqrt{2}$ higher heat load in the small body.
The determination of the SPVG of the particular body shape is discussed extensively by Knauss et al. [69] and Roediger et al. [121]. Pressure measurements were performed at Mach numbers M = 5.94 at T-326 of ITAM and M = 2.5 at IAG. A probe body with a total of 40 pressure tapings with radial spacing of about 0.5 mm was used in order to determine

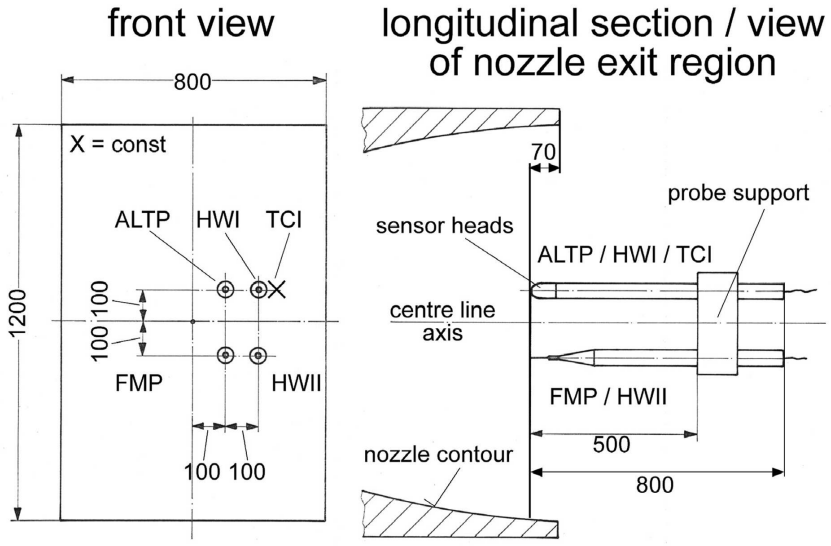

Figure 4.2: Experimental setup in test chamber of SWK.

the surface pressure distribution in the front part of the probe body. The experimentally determined SPVG from the distribution yields $K_{exp} = 9700\,\mathrm{s}^{-1}$. BL computations using an instationary finite volume Euler equation solver of fourth and second order accuracy in space and time results into $K_{comp} = 9200\,\mathrm{s}^{-1}$. The discrepancies of the experimental and computed values can be considered as a measure for the uncertainty in the SPVG.

4.1.3 Experimental Setup.

The operation principle and characteristics of supersonic short duration wind tunnel (Stosswindkanal) of IAG is described by Knauss et al. [70]. The chosen flow conditions are M=2.5 and unit Reynolds number of $Re = 12.6 \times 10^6$ (for steady state I (Z1)) and

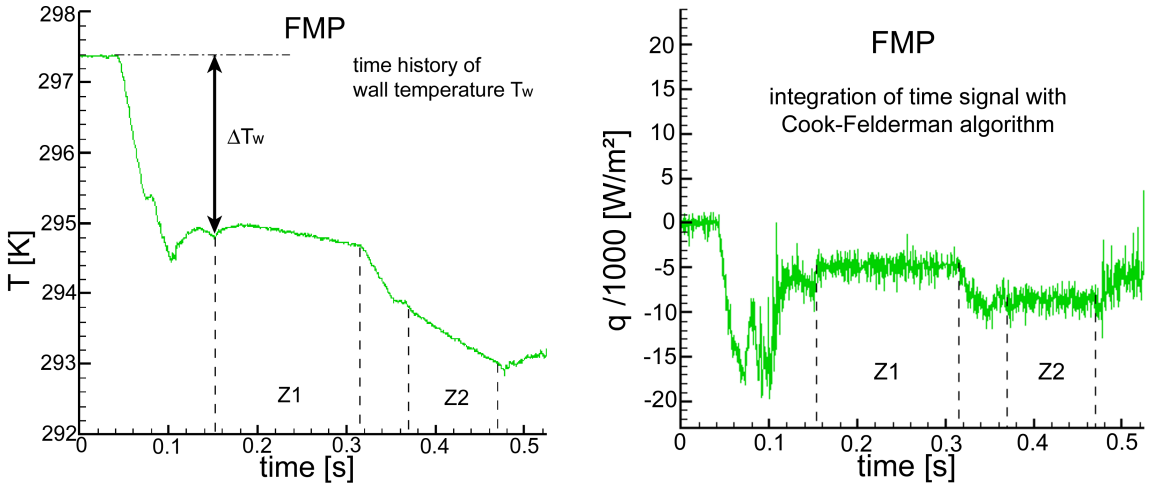

(a)

(b)

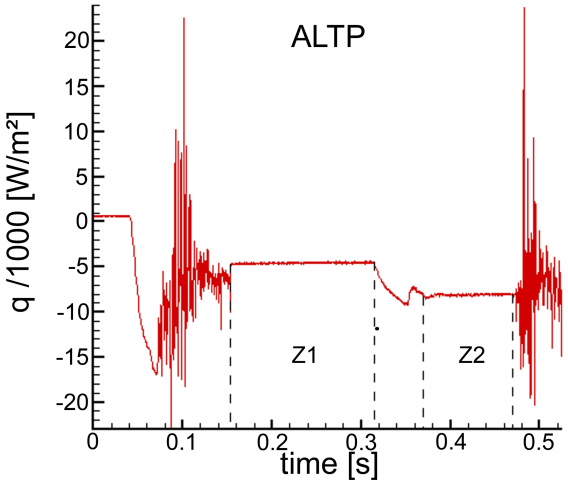

(c)

Figure 4.3: (a) Time signal of FMP, (b) FMP signal after its integration, (c) Time signal of ALTP.

11.4×10^6 (for steady state II (Z2)). Both steady states allow a test duration of 100 ms per run. Figure 4.2 shows the location of the probes in the test section of the tunnel. Two ALTPs (active area $3 \times 6\,\mathrm{mm}^2$) are compared with a DANTEC FMP 55R45 operated by a DANTEC 56C20 temperature plug-in unit of a DANTEC 56C01 CTA system with a constant current of $I = 1\,mA$ and an excitation of $U = 0 - 12\,V$. In addition to the FMP and the ALTP, two hot wire probes (HW I and II) for defining the stagnation temperature as well as a thermocouple (TCI) to measure the initial temperature are mounted in the test section (see Figure 4.2).

4.1.4 Experimental Results.

Typical time signals of the FMP and the ALTP are shown in Figures 4.3(a), (b) and (c), respectively. The time signals show the different flow phases in the test section. After the initial condition, the first steady state (Z1) establishes, followed by the transition phase, the second steady state (Z2) and the final flow breakdown.
The results in Figure 4.3(b) show a good quantitative agreement to the directly measured heat-flux signal of the ALTP (Figure 4.3(c)). The signals also demonstrate the significantly higher temporal resolution of the ALTP. The noise in the calculated heat flux of the FMP is caused by the Cook-Feldermann algorithm [20] and A/D-conversion. Overall, 16 runs with ALTP 1 and 8 runs with ALTP 2 are carried out and processed. Figure 4.4(a) shows the final results for the heat-flux densities of all 24 runs and their comparison to computed values resulting from relation 4.3. The difference of the heat-flux values measured by the

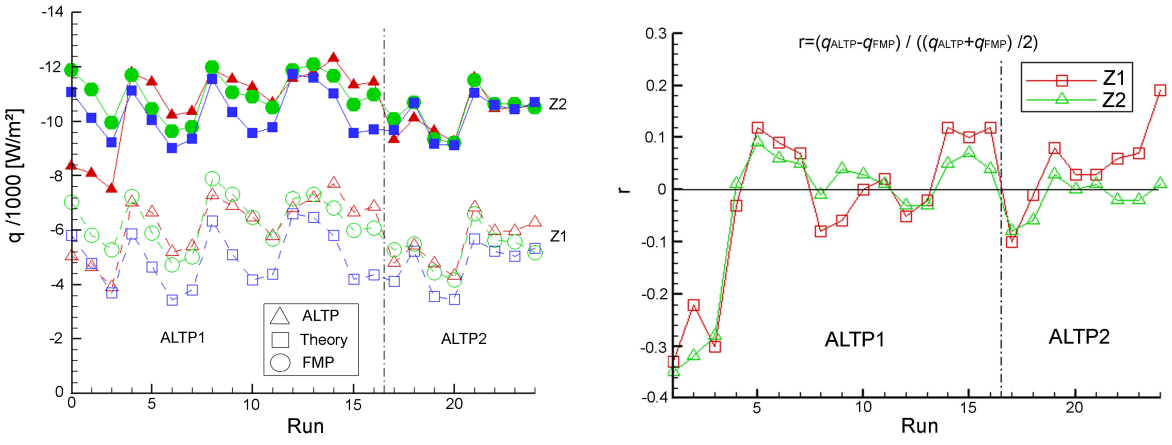

(a) (b)

Figure 4.4: (a) Measured heat-flux densities for ALTP1 and 2, FMP and theory vs. runs, (b) Ratio $r = (q_{ALTP} - q_{FMP})/((q_{ALTP} + q_{FMP})/2)$ of measured heat-flux densities by the different sensors.

individual sensors and normalized by their common mean values in Figure 4.4(b) shows a fairly good agreement for the large amount of runs carried out (difference for most of the runs below 10%) and for the two different ALTPs. The discrepancy in reference to the theoretical heat-flux densities can be deduced from uncertainties in the measured loading temperatures of the driver tube, which is used to define the theoretical stagnation conditions of the flow from the initial conditions.

4.2 Stagnation-Point Heat-Flux Measurements in the High-Enthalpy Plasma Regime

The ALTP is exposed to the high-enthalpy partially or fully ionized plasma in the arcjet plume of the electric thruster TIHTUS. The following section is to provide a demonstration of the ALTP in this harsh regime and at the same time to further characterize the two-stage hybrid electric thruster (see also Böhrk et al. [12]).

4.2.1 Experimental Setup

Plasma source TIHTUS. The two-stage plasma thruster TIHTUS consists of an arcjet thruster (first stage) and an inductively heating afterburner (second stage) and is described in detail in Boehrk et al. [10], [9]. The first stage is formed by the arcjet thruster HIPARC-W [4]. It has a power draw-off up to 100 kW and a converging-diverging, axisymmetrical nozzle with a throat diameter of 6 mm and an exit diameter of 65 mm. The second stage consists of a cylindric 270 mm long discharge tube and a coil of a diameter of 100 mm spun around it as part of a resonance circuit operated at a frequency of f=840 kHz. In induction heating, the power is coupled into the plasma at a near-coil position due to the skin-effect [29]. Power may be coupled into either the arc heated (AH), the inductively heated (RF) stage, or both stages. Each operational condition is therefore referred to as OC $P_{AH}|P_{RF}$-$\dot{m}_{AH}|\dot{m}_{RF}$. As an example, OC 25|25-200|100 refers to the operating condition in which 25 kW are coupled into both, first and second stage while a gas flow rate of 200 mg/s is supplied to the arcjet stage and one of 100 mg/s is supplied to the inductively heated thruster stage. The maximum total pressure is located off axis with 0.85 hPa for the operating point of OC 20|30-300|0. For the same operating condition, a velocity measured with electric time-of-flight probes of 7389±465 m/s and a temperature of 8689±1308 K derived from the latter measurements are reached in the plume axis.

Instrumentation. Radial profiles of heat-flux density q are measured by means of an ALTP mounted in the front surface of a water-cooled blunt body probe of European

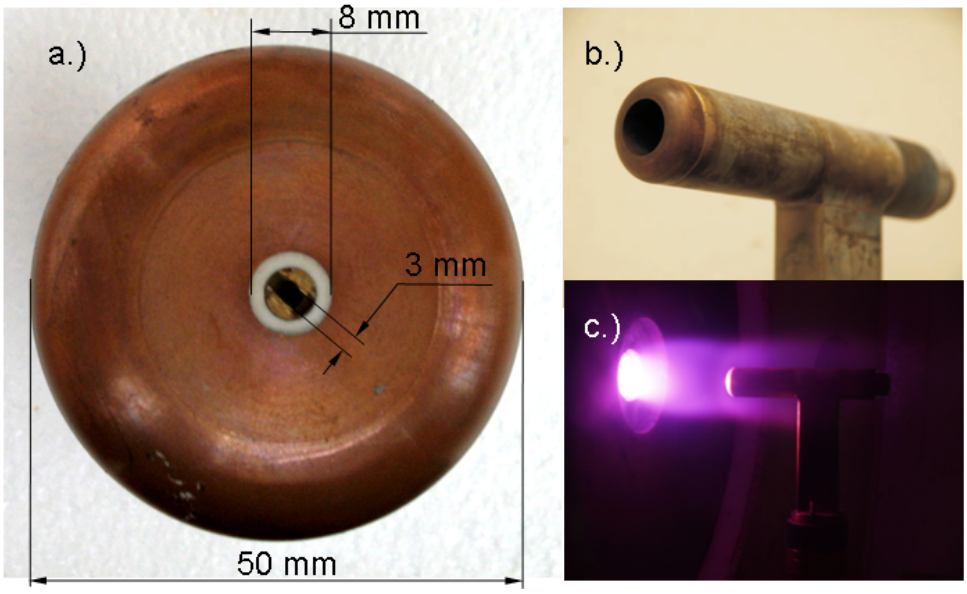

Figure 4.5: Instrumentation: a.) heat-flux probe, b.) total pressure probe and c.) plasma flow with probe of European standard geometry. [12]

standard geometry (flat nose, 50 mm body diameter, rounded edge, see Figure 4.5). In order to determine local enthalpy, the local heat-flux data q are combined with the local Pitot, or total, pressure measurements [10], [9]. The total pressure and heat-flux probe heads can be exchanged with each other. The pressure inlet diameter of the Pitot tube is 26.5 mm. The probes are mounted in a 310 mm-long probe holder with an outer diameter of D=2R=50 mm. The resulting stagnation flow in front of the heat-flux and Pitot probes are consequently identical. The probes are depicted in Figure 4.5.

Total pressure measurements (steady state) are performed at each radial measurement position. For the heat-flux measurement, however, the probe is radially traversed across the plasma plume at constant speeds between 16 and 33 m/s at an axial distance of x=200 mm from the thruster exit. However, the velocity of the traversing is subject to uncertainty. Since a rarefied high-velocity flowing plasma is investigated, the major part of the heat-flux is due to convection. Therefore, it is assumed that the maxima of total pressure and heat flux are located at the same radial position. The traversing velocity can, thus, be scaled by comparison of the heat flux to the total pressure profile.

A cavity calorimeter [11], [54] is used to measure plasma power P_{Pl}. With an error of approximately 9% [11], plasma enthalpy is thus derived as

$$\chi_{Pl,cal} = \frac{P_{Pl}}{\dot{m}} \tag{4.4}$$

4.2.2 Experimental Results

From total pressure and heat-flux measurement, the local mass-specific enthalpy is determined according to an empirical formula of Marvin and Pope [85]. For a wide range of pressures, velocities, and temperatures, the local specific enthalpy can be calculated from a local measurement of the fully catalytic heat flux in the stagnation point and total pressure to a blunt body probe as in

$$\chi_0(r) = \frac{q_{fc}(r)}{K_{Pope}\sqrt{\frac{p_0(r)}{R_{eff}}}}, \tag{4.5}$$

with the effective probe radius R_{eff}=2.3×R (Loehle [79]).

According to Marvin and Pope and their consideration of the boundary layer equations, it is possible to determine local specific enthalpy from heat flux and total pressure. Their assumptions, however, include a frozen boundary layer and a fully catalytic wall. For hydrogen it is unknown how the fully catalytic heat flux q_{fc} is related to the measured heat flux to the silica sensor. The species-dependant Pope-coefficient K_{Pope} of hydrogen is determined from Marvin and Pope [85] to

$$K_{Pope,H_2} = 0.10226\,\mathrm{kW\,kg\,(MJ\,m)^{-1}(m\,Pa)^{-1/2}}. \tag{4.6}$$

The radial measurement data at axial distance x=200 mm of operating condition OC 20|0-300|0 are displayed in Figure 4.6 (a). Due to higher power coupling in condition OC 25|0-200|100, both heat flux and total pressure are higher than in the former operating condition, see Figure 4.6 (b). The total pressure underlies a measurement error of 10%. Thus, a reproduced uncertainty yields 10.5% in the method according to Marvin and Pope [85]. Additionally, they give an error of their semi-empirical method to up to 30 - 40%.

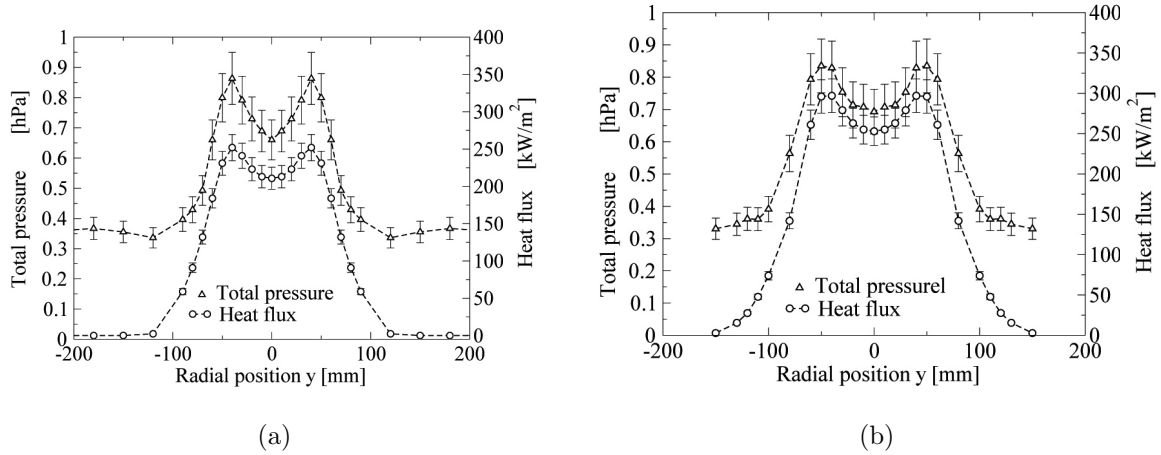

(a) (b)

Figure 4.6: Heat flux and total pressure at (a) OC 20|0-300|0; (b) OC 25|0-200|100. [12]

The value of the plasma enthalpy, derived from calorimetric measurements with the cavity calorimeter and according to Equation 4.4, is determined for the considered operating condition OC 20|0-300|0 to 36.67 MJ/kg. The value corresponding to the result of Equation 4.5 and integrated according to

$$\chi_{Pl} = \int_a \chi \, da = \frac{1}{a} \sum_i \chi_i \, a_i \tag{4.7}$$

yields 31.44 MJ/kg and differs about 14% from the calorimetrically determined enthalpy at the plasma source exit.

It must be kept in mind that due to the uncertainty in the traversing system, the heat-flux profile was assumed to have its maxima concurring with total pressure maxima. Although this seems to be a legitimate assumption, especially since the plasma is flowing at high velocity (>6000 m/s [10]), it shall be mentioned here that equation (4.7) is sensitive to an uncertainty of the plume cross-section a.

At the operating condition of OC 25|0-200|100, the calorimetric measurement yields 36.5 MJ/kg, while the integral of the local measurement results in 30.0 MJ/kg. The values differ about 18% from each other. The values are recalled in Table 4.1. The table shows that in both cases, the results obtained after integration of the local specific enthalpy derived according to Marvin and Pope, indicate lower enthalpy than the calorimetrically measured ones. This deviation can be explained by the unknown relation of the fully catalytic heat flux to the heat flux onto the lowly catalytic active silica coated surface of the ALTP. The hydrogen atoms do not fully recombine at the silica surface, as assumed

	$\chi_{Pl,Kal}$ [MJ/kg]	$\chi_{Pl,Pope}$ [MJ/kg]	dev. [%]
OC 20|0-300|0	36.7	31.4	14.4
OC 25|0-200|100	36.5	30.0	17.8

Table 4.1: Comparison of enthalpy values.

in the theory of Marvin and Pope. For air and copper sensors, this relation is known as q_{fc}=1.2 q_{Cu} (Loehle [79]). In the present case of hydrogen and the silica-coated ALTP, no values are accessible for the behavior relation of the fully catalytic and the lowly catalytic surface. From the few results of the present investigation, taking into account the uncertainties in total pressure, heat flux, the calorimeter measurement and as well as a conservative 40% that Marvin and Pope give for their empiric formulation, the ratio is determined in a first approach to

$$q_{fc} = (1.16 \pm 0.7) \; q_{SiO/SiO_2} \, . \tag{4.8}$$

For accurate enthalpy measurement, however, reliable data of reaction coefficients and energy accommodation coefficients are necessary.

Conclusions. The performance of the ALTP in the high-enthalpy environment of an electric arcjet thruster plume could be successfully demonstrated. It is shown that long-term measurements in the range of a few seconds could be taken providing a radial heat-flux distribution in the plume to the silica surface of the sensor.
In order to verify the measurement data, it was combined with Pitot pressure data so that the locally resolved enthalpy could be derived. The enthalpy integrated across the plume cross-section was then compared to calorimetrically measured plasma enthalpy. The results are good with a deviation of $< 18\%$. The deviation is a result of, among others, missing data for the lowly catalytic sensor surface behavior in hydrogen.

4.3 Transition Studies of a Boundary Layer behind a Moving Shock Wave

The BL formed behind the moving shock wave is studied and the heat transfer measurements are compared with previous theoretical and experimental investigations of the laminar, transitional and turbulent state of the BL (see also Roediger et al. [122]). The ALTP is used to investigate the transition mechanisms from laminar to turbulent in such shock-induced flows. The initial shock tube conditions establish a unit Reynolds number range of more than one order of magnitude, reaching from $0.5 \times 10^6 < Re_{unit}/m < 11 \times 10^6$. The temporal resolution allows the detection of the boundary layer transition not only by a rise of the mean heat-flux density but also by the detection of the increase of the heat-flux fluctuation level.

4.3.1 Theoretical Relations and Overview

A shock wave that travels into a stationary fluid bounded by a wall creates an instationary boundary layer along the wall. In a shock fixed coordinate system, the BL which grows from the foot of the shock can be regarded as quasi-steady. It differs from the usual (stationary) BL in that in this coordinate system the wall moves with a velocity of the shock wave. The shear stress and heat transfer vary with distance from the “leading edge” in the same manner as in the stationary case. Mirels [90] found a solution for the laminar BL equations between the shock wave that moves into a stationary fluid over an infinite

flat plate. An expression, based on Mirels' solution, for the heat transfer rate into the wall is given by Davies and Bernstein [21]:

$$q = s'(0)(T_w - T_r)\frac{c_p}{Pr}\sqrt{\frac{\rho_w \mu_w (u_s - u_2)}{2\, u_s t}} \tag{4.9}$$

where T_w is the wall temperature, T_r the recovery temperature defined by

$$T_r = T_2 \left\{ 1 + r(0)\frac{\gamma - 1}{2} M_2^2 \right\} \tag{4.10}$$

γ the ratio of specific heat capacities and M_2 the flow Mach number behind the shock. $r(0)$ and $s'(0)$ are functions of the BL velocity profiles and the subscript w refers to wall conditions.

The solution shows that the heat flux at a fixed location x into the wall decreases with $t^{-1/2}$, where t is the time after the passing of the shock wave. Later Mirels [91] gave an interpolation formula for $r(0)$ and $s'(0)$ which closely fit his numerical results in the form of

$$s'(0) = 0.489\sqrt{1 + 1.664\Gamma\, Pr^{0.48+0.22\Gamma}} \tag{4.11}$$

and

$$r(0) = Pr^{0.39-0.023\Gamma} \tag{4.12}$$

where $\Gamma = u_s/(u_s - u_2)$, which is equivalent to the density ratio ρ_2/ρ_1 across the shock. The transition from laminar to turbulent occurs within a certain time interval $t_{t,onset}$ to $t_{t,end}$. For a fixed location, the unsteady heat flux into the wall increases significantly during the transition process.

In a turbulent BL, Weatherstone et al. [146] and Mirels [92] estimated the heat flux for a fixed location to decrease proportionally to $t^{-1/5}$. Different power laws can be found in literature as well as different approximations for the heat-flux rate into the wall of a turbulent BL. A review of references concerning this subject is given by Oertel [98] prior to 1966 and by Spence and Woods [136] prior to 1964.

Experimental studies of the laminar and turbulent boundary layer behind a moving shock and the transition process were carried out in various facilities by means of optical methods and wall-mounted probes in supersonic flows. Fundamental optical experiments using Schlieren method [134], streak pictures of tracer particles [39] and interferometric measurements [3], [133] measured the transition location, velocity and density profiles of the laminar, transitional and turbulent boundary layer behind a moving shock for different Mach numbers.

An overview of transient surface temperature and heat-flux measurements prior to 1959 was given by Hartunian et al. [49]. Further experiments on shock tube wall boundary layer transition and comparisons with theoretical estimations can be found in [14], [18],

[21], [26], [83], [93], [115] and [143]. It should be noted that the work of Davies and Bernstein [21] studied the shock-induced boundary layer on a semi-infinite flat plate. In a shock-fixed reference frame, however, the results can be compared with the present investigation as mentioned above.

Definitions. The common definition of the shock-tube Reynolds number, based on laboratory reference coordinates, is

$$Re = \frac{\rho_2 u_2 x}{\mu_2} = \frac{\rho_2 u_2^2 t}{\mu_2} \tag{4.13}$$

where μ_2 is obtained from Sutherland law and the characteristic length x is the distance that a particle travels in the free stream relative to the wall in the time t.
The Stanton number is defined by

$$St = \frac{q}{\rho_2 u_2 c_{p,2}(T_r - T_w)} \tag{4.14}$$

where q is the measured heat-flux density, T_r the recovery temperature and c_p the specific heat at constant pressure. The definition of the transition Reynolds number differs from the Reynolds number defined above (Eqn. 4.13). The relevant characteristic length x_p which describes the distance traveled by a shock induced particle since it was initially set in motion by the shock and reaches the transition point (Hartunian et al. [49]), is used as characteristic distance, here indicated by subscript t:

$$Re_t = \frac{\rho_2 u_2 x_p}{\mu_2} = \frac{\rho_2 u_2^2}{\mu_2} \frac{u_s t}{(u_s - u_2)} \tag{4.15}$$

4.3.2 Experimental Setup

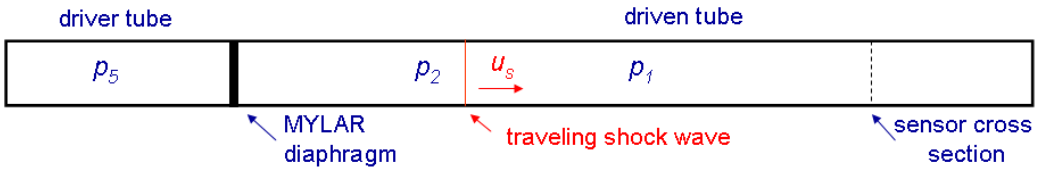

Figure 4.7: Schematic of the shock tube ST70A of ISL.

ST70A facility. The experiments are carried out in the ST70A ISL shock tube (Fig. 4.7). The driver section is 2 m long and separated by a MYLAR diaphragm from a driven section. The tube has an inner diameter of 70 mm with a honed surface in order to

reduce its surface roughness. Connecting elements between the steel tube segments allow 6 sensors to be installed at a defined cross section of the tube as well as some pressure transducers along the driven tube to determine the shock velocity.
For Run 1&2 the driven section is 7 m long and for Run 3, 6.5 m in length. Measurements with a commercial thin-film gauge produced by SWL [102] and two ALTP sensors are carried out at a position 6 m downstream of the MYLAR diaphragm. The sensitivity of the ALTP and the specification of the thin-film gauge are listed in Table 4.2. Low-noise amplifiers (nominal gain 100) are used for the amplification of the ALTP sensor signals. All signals are captured with a sampling rate of 40 MHz and 14-bit resolution.

Sensor (Serial number)	active area $[mm^2]$	Sensitivity s (GAIN=1)	$\sqrt{\rho ck}$ of substrate $[J/(cm^2K\sqrt{s})]$	Resist. $[\Omega]$
ALTP (798) w/o. coating	0.4×2	$182\,\mu V/(W/cm^2)$	0.5246	125
ALTP (797) w. coating	0.4×2	$127\,\mu V/(W/cm^2)$	0.5246	291
Thin Film (P-657)	0.3×0.9	$3852\,\mu V/(Ws^{1/2}/cm^2)$	0.3223	28.67

Table 4.2: Specification of installed ALTP and thin film gauges.

RUN	$M_s[-]$	$u_s[m/s]$	$M_2[-]$	u_2 [m/s]	$T_2[K]$	$\Gamma[-]$	$Re_{unit} \times 10^{-6}[1/m]$
1	1.78	618	0.82	352	443	2.32	0.5
2	2.23	776	1.08	517	547	2.99	0.82
3	3.28	1156	1.43	880	881	4.25	11.3

Table 4.3: Experimental conditions of sample runs.

Experimental Conditions. The characteristics of the instationary BL and the laminar-turbulent transition behind a moving shock are studied and discussed for a unit Reynolds number range between 0.5×10^6 /m and 11.3×10^6 /m. Three sample runs within the Reynolds number regime mentioned are investigated in detail. Their experimental conditions are displayed in Table 4.3. The determined shock velocity and Mach number are indicated by subscript s and the conditions behind the shock outside of the BL are indicated by subscript 2. Run 1 & 2 used nitrogen as driver and driven gas. In Run 3, helium is used as a driver gas in order to generate a faster shock; the driven section is filled with

nitrogen.

4.3.3 Experimental Results

Figure 4.8 and 4.9 show the signal response of the ALTP sensor(s) to the shock passage, representing the time history of the instationary boundary-layer formation. The measuring time of the three runs varies between 1.5 - 7 ms due the different shock velocities and arrival of the reflected shock wave. The laminar and turbulent region can be clearly identified by a significant rise of measured heat-flux density and an increase of the fluctuation level at the same time. The laminar-turbulent transition of Run 3 occurs within the first $100\,\mu$s after the shock passage. Figure 4.10(a) displays an expansion of this time interval revealing the transition process. A thin-film gauge and an uncoated ALTP mounted at the same cross section of the tube are used for comparison in Run 3. Their time signals are also plotted in Figure 4.9. The time signal of the thin film-gauge does not resolve the transition region due to its larger time constant. In the turbulent region, all three sensor readings correlate well in the measured wall heat flux. The heat-flux signal of the thin-film gauge is superimposed by digital noise because this heat-flux history has to be reconstructed out of the temperature time trace by applying the Cook and Felderman algorithm [20]. The signals of both ALTP sensors show a highly resolved time history compared to the thin-film gauge. The scattering of the measured mean heat fluxes lies within 15%. The discrepancies in the mean values and the fluctuations of the time history could be caused by possible non-uniformities in the shock front and the preceding flow due to a slight asymmetric burst of the diaphragm, which violate the assumption of two-dimensional tube flow.

The heat-flux density postulated by the power law for laminar BL development behind a moving shock wave is plotted for comparison in Figure 4.8 and 4.10(a). The time traces of Run 1 and 2 deviate from the expected decay. The discrepancies are possibly caused by disturbances created by casing effects and conduction errors or non-uniformities in the shock front and the preceding flow due to a slight asymmetric burst of the diaphragm.

For Run 3, a laminar BL state can be defined starting immediately behind the shock. It exists only for a very short time interval $\Delta t_L = 11.4\,\mu s$. The existence of a laminar boundary has already been shown experimentally for similar Mach numbers, e.g. Davies and Bernstein [21], Dillon et al. [26] and Hartunian et al. [49], but has never been detected for such a high unit Reynolds number due to the confined time response of the gauges used in these experiments. Therefore, this specific time interval will be studied more precisely in the following.

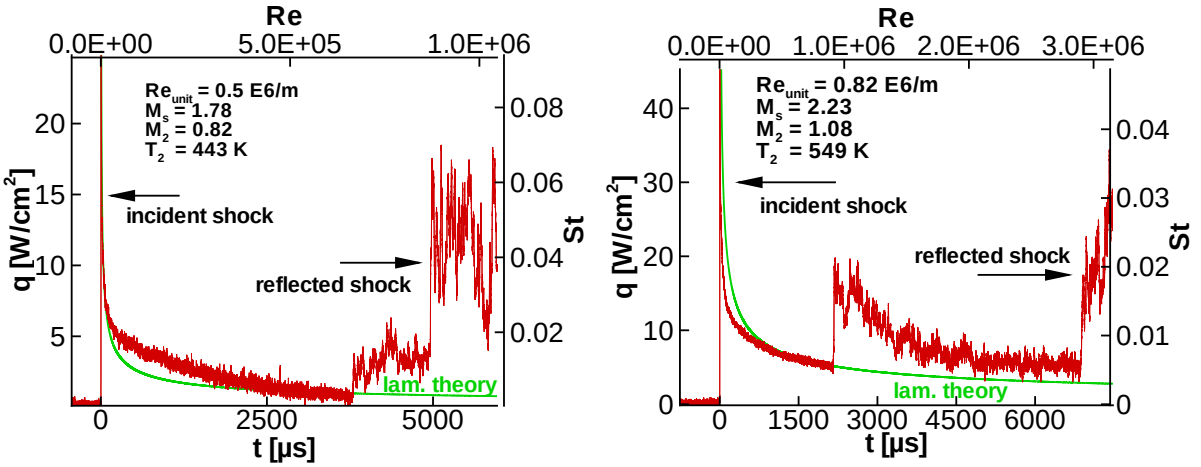

Figure 4.8: ALTP time History of (a) Run 1 and (b) Run 2.

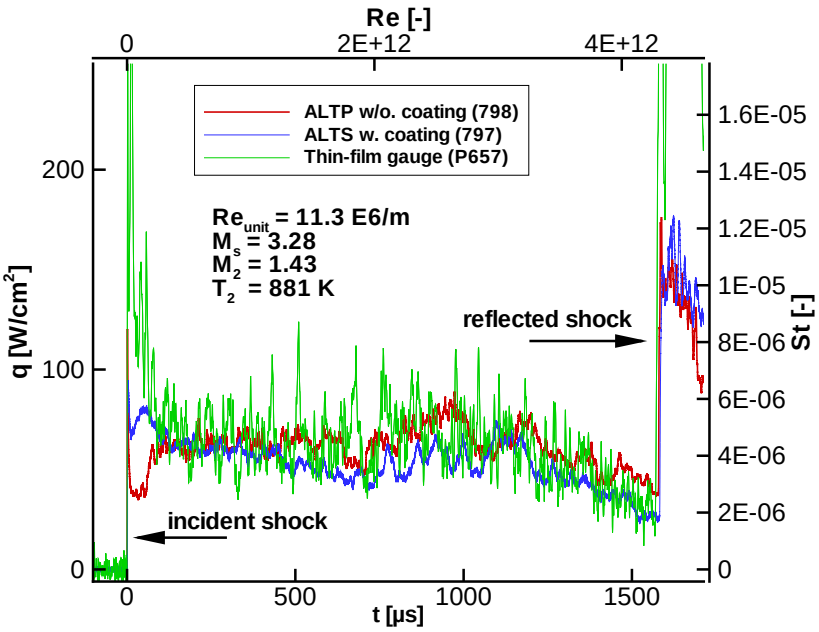

Figure 4.9: ALTPs and thin film time history of Run 3.

According to Mirels' theory, the heat flux of a laminar boundary layer at a fixed location x into the wall decreases with $t^{-1/2}$, thus the laminar region can be identified by the criterion $St\sqrt{Re} = const$. The constant depends on the shock strength $\Gamma = \rho_2/\rho_1$. Figure 4.11 shows a section of the expanded time history, which follows this law, identified by a more or less constant plateau. The uncoated ALTP clearly exhibits a constant region immediately behind the heat-flux peak indicating shock passing. The coated sensor, however, does not reach a plateau like the uncoated one due to its larger time constant. Nevertheless, the slope of the signal decreases in the marked laminar region similar to the uncoated sensor. Consequently, according to the time history of the uncoated sensor,

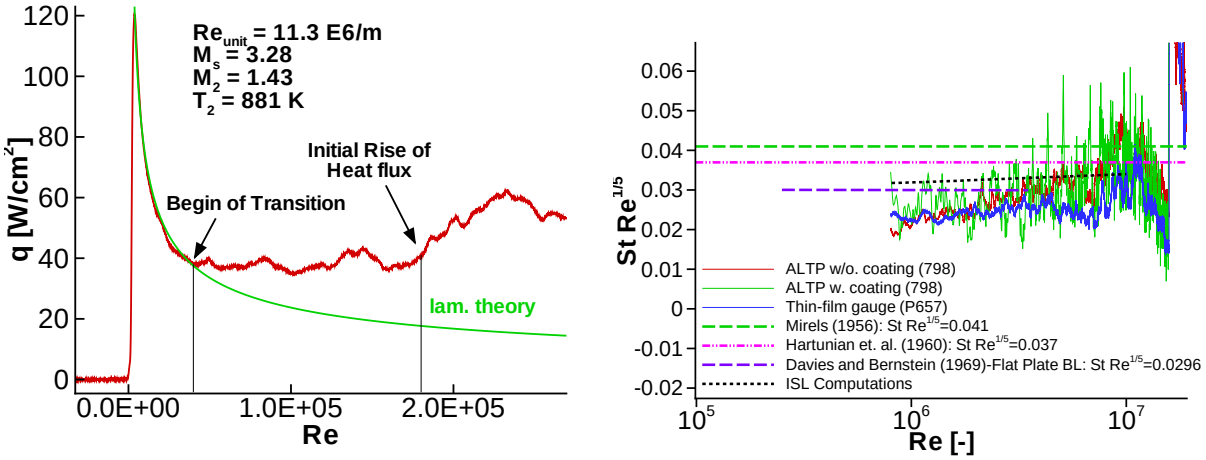

(a) (b)

Figure 4.10: Expansion of sensor signals (Run 3) in (a) laminar and transition region(uncoated ALTP),(b) turbulent region.

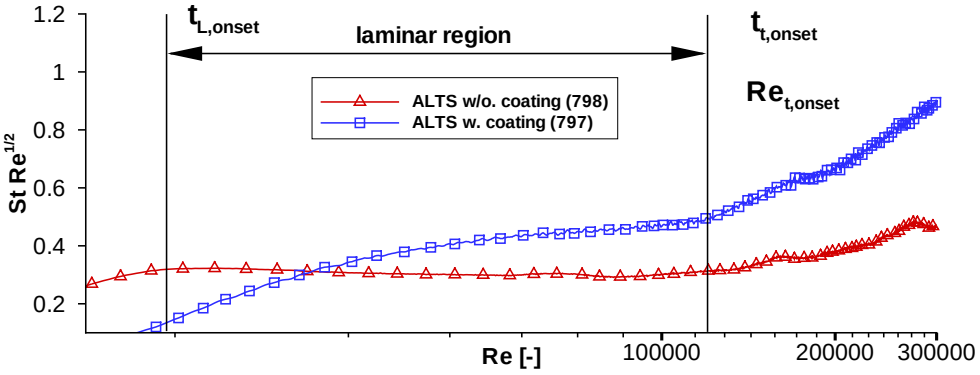

Figure 4.11: Expansion of laminar boundary-layer time history measured by the ALTP sensors (Run 3).

in the time interval $t_L = t_{L,onset} - t_{t,onset}$, a laminar boundary layer state can be defined immediately behind the shock, with a calculated extension of about $x_l = u_2 t_L = 10$ mm. The determined value of the constant in the defined laminar region is approximately $St\sqrt{Re} \approx 0.29$. The constant derived from Mirels' theory using equation 4.9 and the interpolation formulas 4.11 and 4.12 results in $(St\sqrt{Re})_{Mirels} \approx 0.66$. The discrepancy between the present experimental results and Mirels' theory is not clearly understood. Further studies at different shock strengths and unit Reynolds numbers are neccessary.
The onset of a transition process is defined where the trace deviates from the plateau and is marked in Figure 4.11 with a corresponding postulated lowest transition Reynolds number $\mathrm{Re}_{t,onset} \approx 1.25 \times 10^5$ according to the Reynolds number definition in Equation 4.15. The time history in Figure 4.10(a) shows, however, that the heat flux does not increase

immediately from this point but the rise of heat flux is delayed for another 50 μs assigned to $\mathrm{Re}_{t,end} \approx 6.25 \times 10^5$. A similar time history was observed by Davies and Bernstein [21] on a semi-infinite flat plate. The authors noted that as the boundary layer undergoes transition, the heating rate may continue to fall, but at a slower rate. The change in heat flux depends on the relative effectiveness of two opposing tendencies; the local thickening of the boundary layer reduces the wall heat flux while the enhanced mixing tends to increase it. It was stated that a region might exist in which heat flux density remains steady before rising as the turbulence level increases. This statement concurs with the time history found by the uncoated ALTP depicted in Figure 4.10(a). In the definition according to 4.15, a transition Reynolds number range $5.3 \times 10^5 \leq \mathrm{Re}_{p,t} \leq 2.6 \times 10^6$ can be assigned.

In the time traces of Run 1 and 2 (Fig. 4.8), the transition from laminar to turbulent occurs fairly abrupt in a nearly step-like rise of the mean value. A transition Reynolds number of $\mathrm{Re}_t \approx 1.55 \times 10^6$ for Run 1 and $\mathrm{Re}_t \approx 2.7 \times 10^6$ for Run 2 can be defined. The transition scenario clearly differs from the previously discussed time history of Run 3 (Fig. 4.10(a)). The heat-flux rise in Run 1 and 2 seems to produce a weak compression and the formation of a shock wave that could destabilize the instationary BL and accelerate its transition to turbulence. The explanation for the scenario is however speculative and not clearly understood. However, the time traces of all three runs show an increase of the fluctuation level superimposed on the mean value already within the progression of the laminar BL. The heat-flux fluctuations seem to rise to a certain level in the laminar region before the turbulent state is reached after transition.

A final comparison of the observed transition Reynolds number intervals of all three runs with correlation data presented by Hartunian et al. (Figure 2 in [49]) show a good match for the present shock strengths of Run 1 to 3 equivalent to $\mathrm{T}_w/\mathrm{T}_2 = 0.34$, 0.53 and 0.66, respectively.

In the turbulent boundary layer, the heat flux decays with $t^{-1/5}$. Thus the time signal should evolve into a constant plateau for $StRe^{1/5} = const.$ Sometimes a one-seventh power law is more suitable for the transitional region and for lower Mach numbers as already stated by Hartunian et al. [49], but to consistently follow his assumption $St\,Re^{1/5}$ versus Re is plotted in Figure 4.10(b). The *constant* again depends on the shock strength. Various theoretical and experimental values have been found by other authors and are added in Figure 4.10(b) for comparison with the time history of Run 3.

As we can see in the time history of this run, the "defined *constant*" is slightly lower compared to the experimental value given by Hartunian et al. [49] and Mirels' theoretical *constant* [92]. Numerical investigations (see Knauss et al. [71], Srulijes and Seiler [137]) show that a lower exponent for the power law is more suitable to describe the develop-

ment of the turbulent BL and concurrence of the computed heat-flux densities with the experimental values is better with increasing time. The time trace of a thin-film gauge shows a global behavior similar to the two ALTP sensors and independently confirms the ALTP measurements.

Conclusions. Highly time-resolved heat-transfer measurements in the instationary BL behind an incident shock wave are carried out by means of the ALTP. The existence of a laminar BL is found for the first time in a unit Reynolds number range up to 11×10^6/m. The time histories even resolve the progression of the fluctuation level superimposed on the mean heat flux of the laminar BL. Theoretical predictions for the laminar BL developments are in good agreement with experimental results. The observed transition scenarios seem to differ within the investigated unit Reynolds number regimes. For $\mathrm{Re}_{unit} \approx 0.5 \times 10^6$/m and 0.8×10^6/m, the transition from laminar to turbulent occurs as a fast, step-like rise of the mean value. In contrast, the laminar state during the first 11 μs for $\mathrm{Re}_{unit} \approx 11.3 \times 10^{-6}$/m is followed by a constant heat-flux history of about 50μs before the heat flux suddenly increases. The results might indicate two different transition mechanisms encountered in the instationary BL behind a moving shock wave.

4.4 Dynamic Response Evaluation by a Passing Shock Wave

Besides the study of the transition mechanisms of the BL formed behind the moving shock wave, such a passing of a shock allows to evaluate the dynamic response of the ALTP by its response characteristics. A shock wave creates a very sharp step rise in heat flux that can be used for the investigation of dynamic properties and estimation of time responses of wall-mounted sensors. A passing shock wave has several favorable characteristics: (i) The incident shock wave produces a step-like change in heat flux in a convection environment as well as in the emission characteristics of the prevailing gas. (ii) The formation of the shock wave and the developing BL can be regarded mainly as two-dimensional assuming a fairly symmetric burst of the diaphragm. Thus, the response of different sensors arranged in one circumference of a tube cross-section can be compared simultaneously. (iii) The boundary conditions of the experiments are fairly repeatable and easy to measure. A passing shock wave was used to investigate several gauges in the past [42], [50], [58], [115]. For a fast enough traveling shock wave, the harmonic analysis of the response signal results into a AFR characteristic similar to the one resulting from incident laser radiation presented in section 2.8. The comparison of AFR characteristics reveals the fundamental

differences and uncertainties in convective and radiative excitation, respectively.

4.4.1 Experimental Setup

Instrumentation. The experiments are carried out in the ISL shock tube ST70A in a similar setup as already described in section 4.3.2. The active size of all ALTPs is $0.4 \times 2\,\mathrm{mm}^2$ (within certain manufacturing tolerances). All gauges are installed in one cross section 6 m downstream of the diaphragm. Their detailed specifications can be found in Table 4.4. Low-noise amplifiers (nominal Gain 100) and a sampling rate of 40 MHz and 14 bit resolution are used to capture the ALTP signals.

Position [°]	ALTP (Serial number)	coating [nm]	Sensitivity s (incl. absorpt.) [μV/(W/cm^2)]	Resistance [Ω]
Series 1				
60	798	none	182	125
240	797	200	170.9	291
Series 2				
60	1004	none	79	86.1
120	1008	100	81	137
180	1010	none	119	251
240	797	200	155.5	751
300	1006	100	79	50.0
Series 3 (only ALTPs listed that were replaced in reference to Series 2)				
240	1011	none	106	113
Series 4 (only ALTPs listed that were replaced in reference to Series 2)				
60	1007	100	135	50.9
240	1005	100	99	70.5

Table 4.4: Specification of installed ALTPs.

Experimental conditions. Series 1 represents here the detailed investigation of the response characteristics of Run 3 studied in the previous section 4.3. The conditions given in Table 4.3 produce a fast enough traveling shock wave that allows the evaluation of the dynamic properties of the installed ALTPs.
Series 2-4 consist of an overall of 11 runs with conditions similar to the one of series 1. The nominal initial conditions of all 11 runs were kept alike and the mean values and their

standard deviation given in Table 4.5 document the good repeatability of the experimental conditions in the shock tube.

$M_s[-]$	u_s [m/s]	$M_2[-]$	u_2 [m/s]	$T_2[K]$	$\Gamma[-]$	$\mathrm{Re}_{unit}[1/m] \times 10^{-6}$
3.46 ± 0.11	1194 ± 37	1.46 ± 0.02	912 ± 33	964 ± 46	4.23 ± 0.08	11.15 ± 0.34

Table 4.5: Average experimental conditions (mean value, standard deviation) of runs of series 2-4.

4.4.2 Experimental Results

Series 1. Figure 4.12(a) shows a magnification of the signal response of the two ALTPs in Figure 4.9. The scale is plotted in microseconds and the data points are marked for a 40 MHz sampling rate (no filtering has been applied!). The initial slope of the signal shows the shock passing over the sensor ($t < 0.35\,\mu s$) before it significantly increases and the heat flux reaches a maximum at $t = 1.2\,\mu s$ for the uncoated sensor and $t = 3\,\mu s$ for the 200 nm-coated sensor with peak values of 120 and 95 W/cm^2, respectively. The measured time of the shock passing corresponds exactly to the time that can be calculated from the shock speed u_s and the width of the sensor normal to the shock front (0.4 mm). The difference in the rising slope between the 200 nm-coated and uncoated sensor clearly shows the increase in response time due to coating. The characteristic sharp rise of the signals can be deduced from the physical phenomena developing immediately behind the passing of the shock wave. On the one hand, the peak results from the very thin initial BL thickness behind the shock, causing a large temperature gradient at the wall and leading consequently to a considerable convective heat load. On the other hand, radiative processes immediately behind the shock front could lead to a radiative contribution in the thermoelectric signal, which is determined by the gas temperature T_2 behind the incident shock wave. In the present experiments, translatory and rotational degrees of freedom are excited as well as the rotational degrees to some extent since nitrogen is used as the driven gas. At $M_s = 3.28$, all three degrees of freedom are practically in thermodynamic equilibrium, where the translatory, the rotational and the vibrational temperatures are equal to T_2. Dissociation and ionization can be excluded for the moderate shock Mach number $M_s = 3.28$ with a low shock strength. One way to separate the radiative and convective components could be performed by simultaneous spectroscopic measurements in the shock BL.

The time constants of the 200 nm-coated and uncoated sensor can be estimated from the

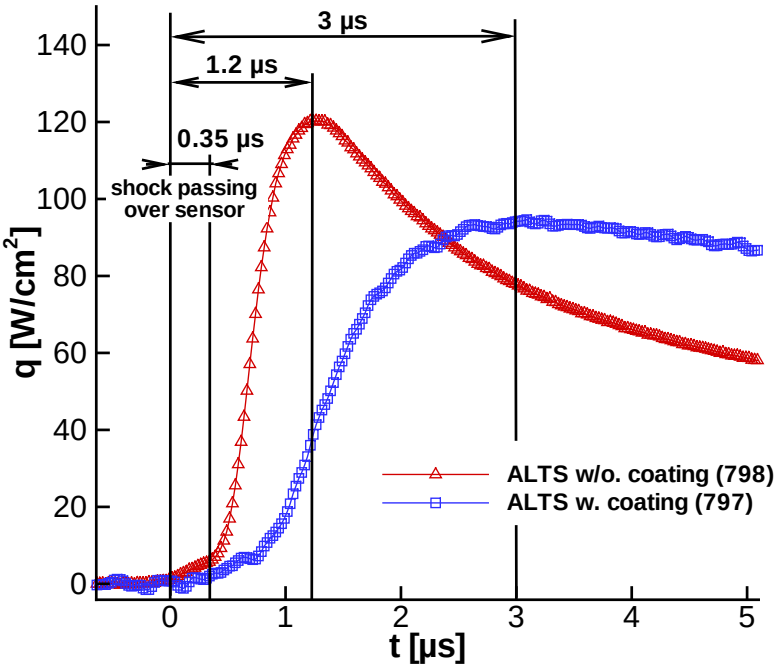

(a)

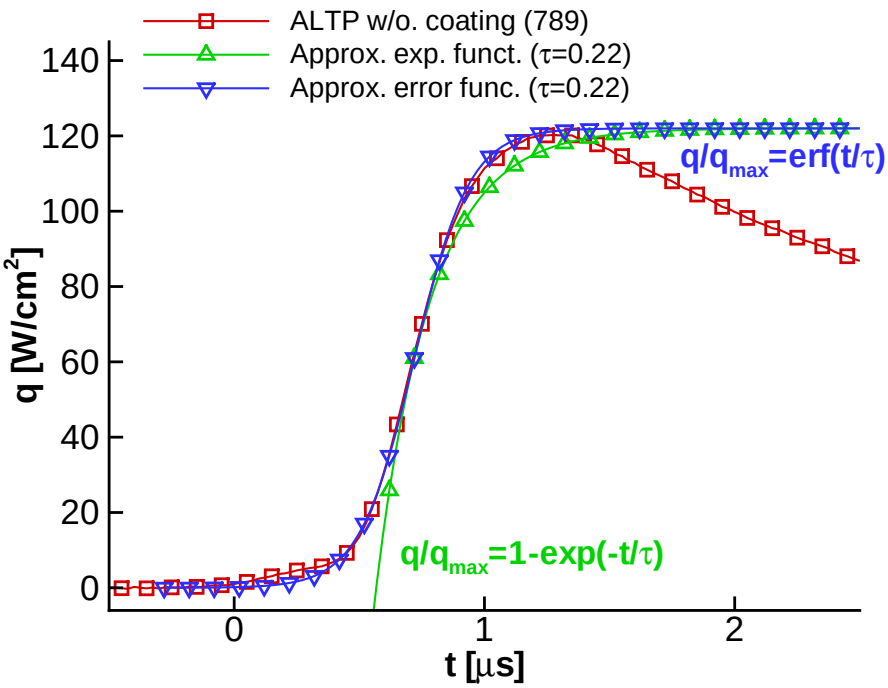

(b)

Figure 4.12: (a) Response of coated (200nm) and uncoated ALTP to the incident shock wave; (b) Approximation of the time history by error and exponential function.

time history in Figure 4.12(b). Holmberg and Diller [58] characterized the response of their sensor from the numerical modelling as "a first order exponential rise". Figure 4.12(b) shows, however, that an approximation by an error function seems to be more suitable,

$$\frac{q}{q_{max}} = erf\left(\frac{t}{\tau}\right) \tag{4.16}$$

leading to a time constant of $\tau_{uc} = 0.22\mu$s for the uncoated sensor and $\tau_{200nm} = 0.55\mu$s for the 200 nm-coated one. The time constants obtained are in the range as predicted from theory and dynamic laser calibration in section 2.8.

Series 2-4. A more exact way to display dynamic properties is their representation as AFR characteristic. In the following experiments, several ALTPs with and without protective coating are compared by simultaneous measurements in one cross section of the shock tube. The different test series reveal the repeatability of the response evaluation

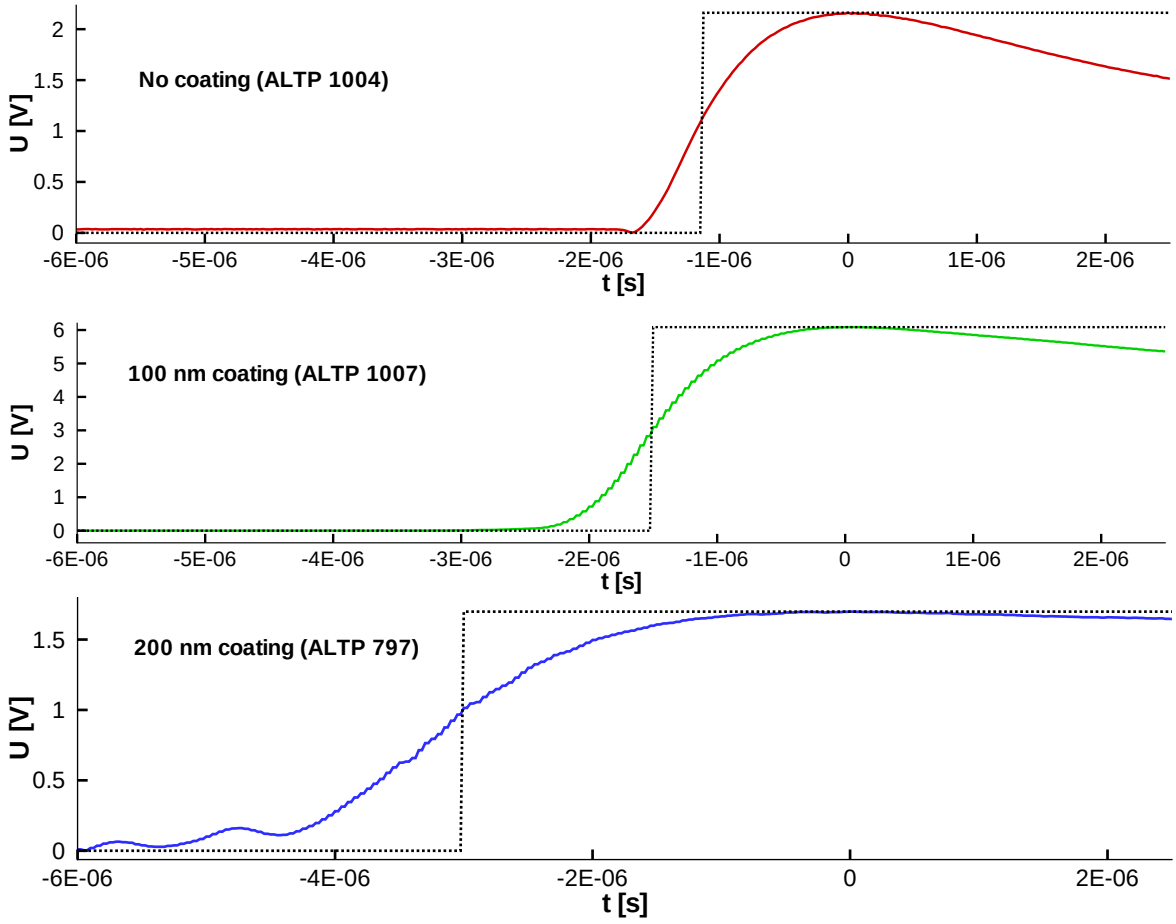

Figure 4.13: Simultaneously measured response of ALTP without coating, 100nm-coating and 200nm-coating.

by a passing shock wave and show the scattering of the AFR characteristics of ALTPs without coating and nominal equally sized protective coating. Hence, this study gives an insight into the manufacturing tolerances of the thickness of the ALTP film and its coating.

Figure 4.13 shows the signal response of ALTPs without coating, 100 nm- and 200 nm-coating, respectively, obtained in one simultaneous measurement. Slight off-center positioning of the active film due to manufacturing tolerances leads to a temporal response off-set in the simultaneous measurements. Therefore, the peak values are used as references for the comparison. It can be seen that the response time increases from $\sim 1.6\,\mu$s for the ALTP without coating (1004) to $\sim 4.3\,\mu$s for the ALTP with 200 nm coating (797). It should be noted that the ALTP with 200 nm coating (797) is the same as used in Series 1. The increase in response time might be deduced from the degradation of the dynamic properties of the ALTP due to aging. The measurements of series 2-4 were carried out approximately 2.5 years past the initial series 1 and the ohmic resistance of the gauge increased from 291 to 751 Ω.

The estimated response times (Fig. 4.13) confirm the expected qualitative rise of the response times with increasing thickness of the protective coating. In the following, the AFR characteristics resulting from the harmonic analysis of the step responses will be used for more precise comparisons.

Figures 4.14(a-f) show the AFR characteristics of several ALTP sensors without coating, 100 nm-, and 200 nm-coating obtained in successive shock-wave evaluations. First of all, the scattering of the dynamic properties of ALTPs with specified protective coatings of equal thickness is clearly visible. The scattering results from the uncertainty of the film thickness of each single sensor, the uncertainty of thickness of the coating and the limited repeatability of the experimental conditions. The results of the shock-tube evaluation are compared with AFRs obtained from dynamic calibration by exposure to a sinusoidally modulated laser beam (sec. 2.8) for each single sensor used in of Figure 4.14 (left column). Furthermore, the experimental results are compared with theoretical computations for a variation of film and coating thickness in Figures 4.14 (right column).

Figure 4.14(a) displays the AFR of three ALTPs without protective coating resulting from shock wave experiments. For a prescribed attenuation of -3 dB (equivalent to $A_{ALTP}/A_{ref} = 0.71$), the assigned frequency varies between $f \approx 290$ - 375 kHz. A systematic overprediction of the attenuation by the laser calibration procedure in reference to the evaluation by a passing shock wave can be clearly seen. It must be noted that the uncertainty of the dynamic laser beam calibration increases with rising prescribed frequency because of the decaying signal to noise ratio of the ALTP. The limiting ratio depends on the sensitivity of each gauge and once the limit is trespassed the AFR stag-

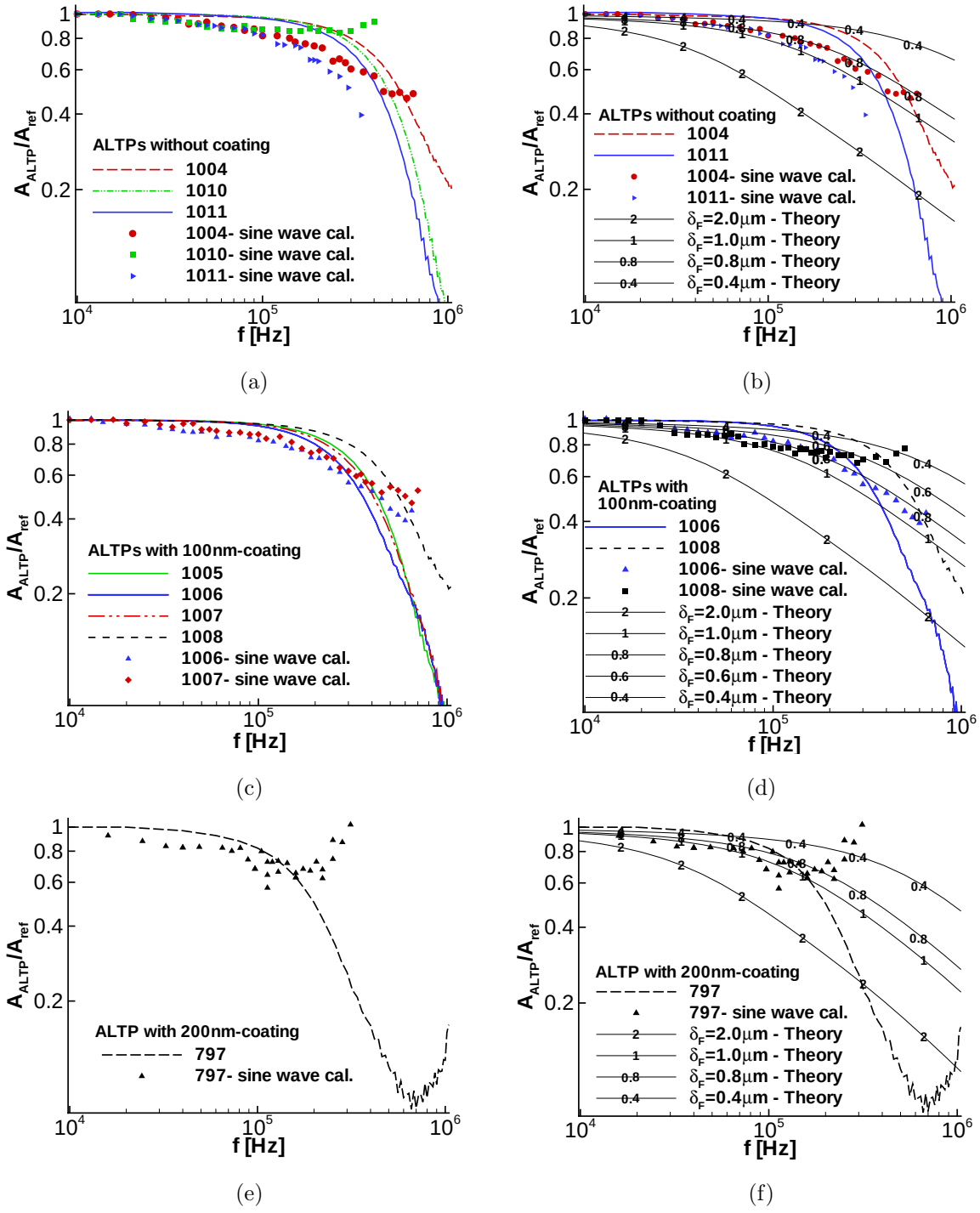

Figure 4.14: Comparison of AFR characteristics: (left column) obtained from passing shock wave response and dynamic laser calibration, (right column) experimental vs. theoretical results, for a variation of thickness of protective coating: (a+b) without coating, (c+d) 100 nm coating, (e+f) 200 nm coating.

nates at a certain level and A_{ALTP}/A_{ref} starts to rise afterwards (as seen for ALTP 1010 in Fig. 4.14(a)). Further comments on the uncertainty of this procedure can be found in

section 2.8. Altogether, there seems to be a systematic difference in the laser-radiation based and the convectively-dominated shock tube calibration procedure. Yet qualitatively both procedures predict the same trend in attenuation, the attenuation of sensor 1011 is stronger than the one of sensor 1004 (sensor 1010 already drops below the signal to noise ratio limit for f$\approx$100kHz). Figure 4.14(b) compares the experimental AFR ranges with theoretical estimations for a variation of film thickness. A good agreement of the laser calibration and theoretical results for a film thickness varying between $0.8\,\mu\text{m} \leq \delta_F \leq 1\,\mu\text{m}$ can be found in a frequency range up to $\sim$300 and 500 kHz, respectively. These film thicknesses lie within the manufacturing tolerances of the ALTP film between 0.4 and 1 μm. For higher frequencies, the theoretical predictions show slower attenuation. This could be linked to the simplified theoretical model of the ALTP slab (sec. 2.8), which does not account for any thermal contact resistance between the layers.
The AFRs obtained from the shock-wave evaluation do not match the theoretical predictions in the entire frequency range. A possible reason for this discrepancy could be related to the finite time of the passing of the shock. The passing time is only slightly smaller than the time constant of the ALTP. However, the creation of faster shock was not possible in the actual shock tube.
Figure 4.14(c) displays the AFRs of four ALTPs with 100 nm-coating resulting from shock-wave experiments. The frequency range assigned to an attenuation of -3 dB lies within f$\approx$245 - 375 kHz. The AFR of an ALTP with 200 nm-coating is shown in Figure 4.14(e). The -3 dB drop-off is significantly reduced to a value of f$\approx$135 kHz. The comparison of the AFRs of the coated sensors with theoretical estimations in Figures 4.14(d) and (f) exhibits similar discrepancies between the theoretical AFRs and the ones attained from passing shock-wave responses as observed for ALTPs without coating. A film thickness that can be deduced from the laser-radiation AFRs in reference to the computations lies within $0.6\,\mu\text{m} \leq \delta_F \leq 1\mu$m matching the manufacturing tolerances.

It is important to note that a direct comparison of the laser radiation based calibration with the convective response is strictly speaking not legitimate because the protective coating is transparent for the wavelength of the diode laser with an emission in the 680 nm range. Hence, the calibration characterizes only the ALTP film without protective coating. The comparison should allow the separation of the effect of the coating and the actual film thickness by means of the comparison of the AFR characteristics obtained from both experimental dynamic calibration procedures. Unfortunately, the accuracy of the laser-based calibration procedure is insufficient, especially in the higher frequency range. The ratio of AFR characteristics of the laser radiation based calibration and the convective response for a variation of film thickness is shown in Figure 4.15(a). The ratios show that a consistent quantitative separation of the influence of the protective coating

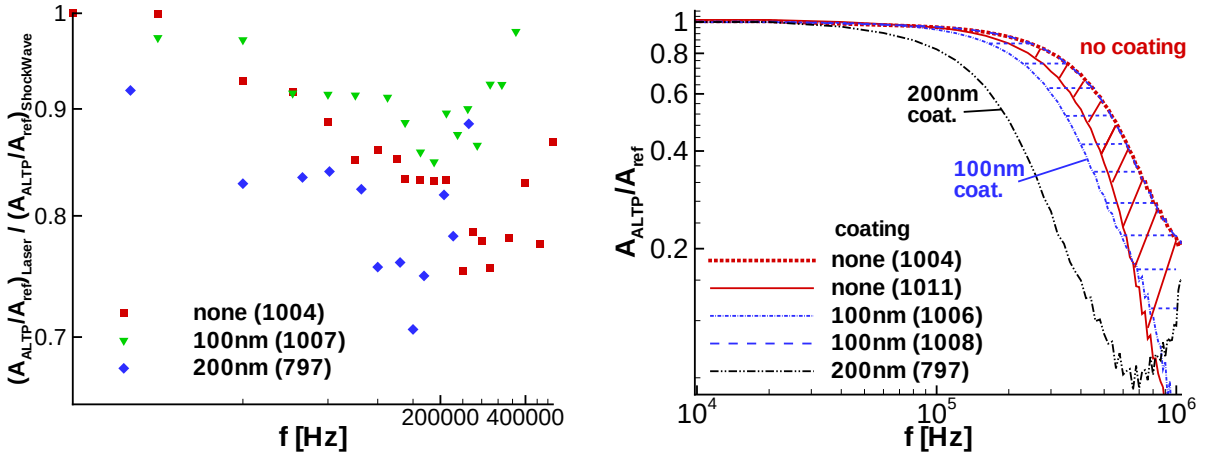

(a) (b)

Figure 4.15: (a) Ratios of AFR characteristics obtained from laser calibration and passing shock wave evaluation, (b) Comparison of AFR ranges for a variation of coating thickness.

is not possible with the current setup and further improvements have to be made.
Figure 4.15(b) shows the ranges that are spanned by the ALTPs with the best and poorest AFRs in Figures 4.14 obtained by shock-wave evaluation. The deterioration of the dynamic characteristics with increasing thickness of the protective coating appears not to be linear. The -3 dB drop-off for a sensor with 200 nm-coating is significantly lower than the one of a film with 100 nm-coating. For sensors with 100 nm-coating, the dynamic properties seem to deteriorate only to a small extent with respect to sensors without coating. The shaded areas indicate that sensors with 100 nm coating can reach similar dynamic characteristics as sensors without coating. The effect of film thickness seems to be more dominant for sensors with such a thickness of protective coating. Therefore, protective coatings in a range of 100 nm appear to be optimal in order to maintain the dynamic properties of the ALTP and to stabilize the sensitivity of the film at the same time.

Conclusions. The dynamic properties of the ALTP are characterized by monitoring its response to a passing shock. The passing of the shock wave could be resolved in an interval of 0.35 μs. The successive convective heat-flux rise within less than 1 μs demonstrates that the ALTP gauge without protective coating has a frequency response of almost 1 MHz. A systematic investigation of ALTPs with differently sized protective coatings is carried out. A coating with a thickness of $\sim$100 nm is found to be an optimal compromise between the two opposing requirements of a stable sensitivity of the ALTP and a high temporal resolution. The compilation of AFR characteristics of several ALTPs with nominal equally sized coating also provide a basis for statistical tolerances in the manufacturing procedure.

Furthermore, the AFR characteristics obtained from dynamic laser calibration and theory are compared with the mainly convectively produced response to the passing shock-wave. The results show similar qualitative results of both experimental techniques but also reveal systematic differences between the the two procedures based on radiation and convection, respectively. Specific reasons for the discrepancies are identified and uncertainties in the procedures in reference to the theoretical modeling are discussed. Both procedures can be improved. The method based on radiation would benefit from a larger laser-beam intensity resulting into a higher signal to noise ratio of the modulated diode laser at 680 nm. Another approach would be the use of a high-speed shutter (opto-acoustic modulator, Bragg cell) for fast beam deflection of a continuous CO_2-laser beam at 10.6 μm. The method based on convection can be improved by an increase of the shock velocity of the passing shock wave.